Si Photonic Waveguides with Broken Symmetries:
Applications from Modulators to Quantum Simulations

Shinichi Saito[1]*, Isao Tomita[1,2], Moïse Sotto[1], Kapil Debnath[1,3], James Byers[1], Abdelrahman Z. Al-Attili[1], Daniel Burt[1], Muhammad K. Husain[1], Hideo Arimoto[1], Kouta Ibukuro[1], Martin Charlton[1], David J. Thomson[1], Weiwei Zhang[1], Bigeng Chen[1], Frederic Y. Gardes[1], Graham T. Reed[1], and Harvey N. Rutt[1]

[1]Faculty of Engineering and Physical Sciences, University of Southampton, Southampton SO17 1BJ, UK
[2]Department of Electrical & Computer Engineering, National Institute of Technology, Gifu College, 2236-2 Kamimakuwa, Motosu, Gifu 501-0495, Japan
[3]Department of Electronics & Electrical Communication Engineering, Indian Institute of Technology, Kharagpur, West bengal 721302, India

Symmetries of waveguides determine fundamental properties of photons such as mode profiles, polarisation, and effective refractive indexes as well as practical properties affecting the propagation loss. Here, we review our recent progress on manipulating symmetries of silicon (Si) photonic waveguides. Starting from the strategic choice of Si-On-Insulator (SOI) wafer specifications, we established the process technologies to fabricate Si wire and slot waveguides with atomically-flat interfaces, defined by Si (111) planes. These waveguides have relatively low propagation loss ($\sim$ 1 dB/cm), even though they were fabricated in a university line. By combining patterning and re-growth of deposited amorphous Si, we also fabricated an Si slot waveguide with a nano-meter-scale vertical oxide layer, which is useful for optical modulators and various sensing applications. We also fabricated a horizontal slot waveguide using our manually bonded double-SOI substrate. The self-limited alkali-wet-etching allowed us to pattern the bottom SOI layer on top of the top SOI layer, by properly designing the mask to align along the mirror asymmetric Si (110) surface, allowing to access to top and bottom SOI layers individually through connected multiple-fin arrays. The patterning technique can be readily applicable to the other platform such as Si/LiNbO$_3$-hybrid wafers, and we discuss our design of electro-optic (EO) modulator towards zero-power consumptions. We also investigate photonic crystal waveguides with broken mirror symmetries. By manipulating the mismatch between adjacent photonic crystals across the waveguide made of line defects, we could continuously control the band gap of the photonic crystals. Moreover, the phase profiles of modes exhibited photonic graphene and poly-acetylene shapes, made of optical vortices with optical orbital angular momentum (OAM). This shows that the most energetically favourable configuration of a photonic material under the triangular lattice is topologically equivalent to an organic material. We discuss the potential for the photonic organic chemistry and possible applications in quantum technologies.

1. Introduction

Silicon and oxygen are 2 most abundant materials on the surface of the crust of the earth, which would not be just a coincidence that these materials play dominant roles for Si-based electronics and silica (SiO$_2$)-based fibre optics.[1–4] The continuous scaling of feature size of Complementary-Metal-Oxide-Semiconductor (CMOS) Field-Effect-Transistors (FETs), called Moore's law,[5] was the guiding principle for almost half-century and still the significant efforts are being made to establish the technology node with the smaller feature size. However, the physical scaling down cannot be continued forever both fundamentally and economically, and only a few global industries can continue to invest, which led the suspension of the International Technology Roadmap of Semiconductor (ITRS).[6] In fact, the clock speed of the latest Micro-Processor-Unit (MPU) is not significantly improved compared with that of a decade ago, although the overall performance of the MPU is enhanced with the help of multi-core processing architecture. The end of the scaling, or more precisely, the slow-down of the scaling does not mean that a new platform technology with novel device operation principle or new materials can suddenly take over Si CMOS technologies. Nevertheless, CMOS process technologies can be readily applicable to other devices such as Micro-Electro-Mechanical Systems (MEMS) and Si photonics.[7–15] In particular, the global market of Si photonics is increasing with the annual growth rate of $\sim 20\%$[16] due to the increased demands for transceivers of active optical cables in data centres. Si

Table I. Fundamental properties of an electron and a photon as an elementary particle. The charge and mass of an electron are e and m_e, respectively, and the velocity is determined by the mobility, μ, and the electric field, E_{el} in the drift-diffusion regime below the saturation velocity, v_{sat}. The velocity of a photon is c in the vacuum, and it reduces to $v = c/n$ in a material with the refractive index of n. A photon has spin 1 degree of freedom (in the unit of the Dirac constant, $\hbar = h/(2\pi)$, with the Plank constant, h), which has potentially three magnetic states, but only two polarisation states (horizontal/vertical, left/right, or diagonal/anti-diagonal) can be realised due to the transversality of electro-magnetic waves (with no longitudinal component). Electrons and photons have both particle and wave characters, following quantum mechanics.
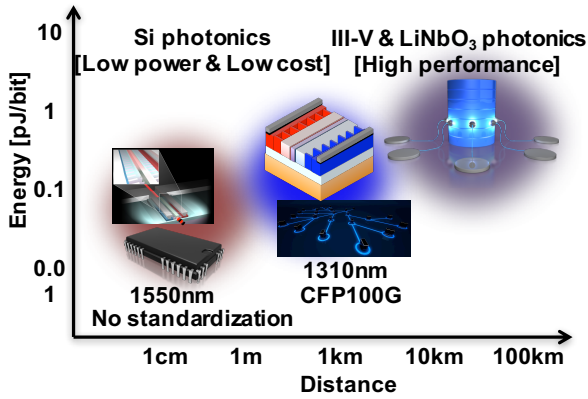
Character	Electron	Photon
Charge [C]	e	0
Spin [$\hbar$]	$\frac{1}{2}$	1 (Two polarisation states)
Mass [kg]	m_e	0
Velocity [cm/s]	μE_{el}	c
Statistics	Fermi-Dirac	Bose-Einstein
Coherence	Only in a superconductor	Ubiquitously available
Devices	CMOS, $\cdots$	Lasers, detectors, $\cdots$
Applications	Logic, Memory, $\cdots$	Transmission, Display, $\cdots$

photonics is also promising for Light-Detection-and-Ranging (LIDAR)[17,18] towards autonomous vehicles, biomedial sensing,[19,20] and applications in quantum technologies.[21–25]

The main advantage to use photons instead of electrons is the absence of the Ohmic dissipation during the propagation due to the lack of charge of a photon (Table I). The propagation loss in a fibre could be as low as 0.14 dB/km,[26] which allows long-distance communications at high data transmis-
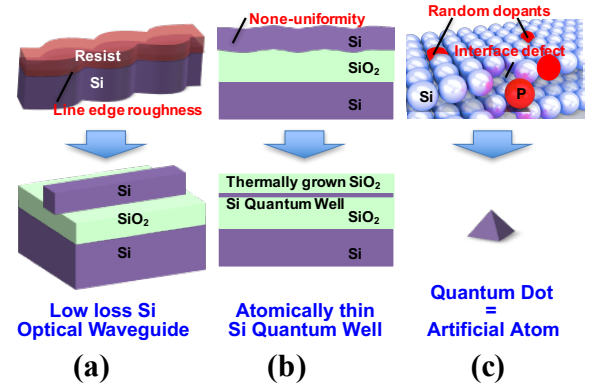
sion rate.[27] Obviously, the conversions from Electrical-to-Optical (EO) and inverted Optical-to-Electrical (OE) signals are required in order to use photons for communications.[27] But, the superb low propagation loss in an optical fibre allows the sufficient loss budget to compensate the disadvantage of these conversions. Therefore, photon-based data transmission has an advantage in a longer distance communication in general.[27] The extensive uses of networks for massive data transmissions are pushing this boundary between fibre optics and copper (Cu) based electronic wiring towards the shorter distance.[28] Vertical-Cavity Surface-Emitting Lasers (VCSEL) and Si photonics[7–15] are innovative solutions to revolutionise optical interconnections to support increasing demands such as high-definition video-subscriptions and cloud computing (Fig. 1).
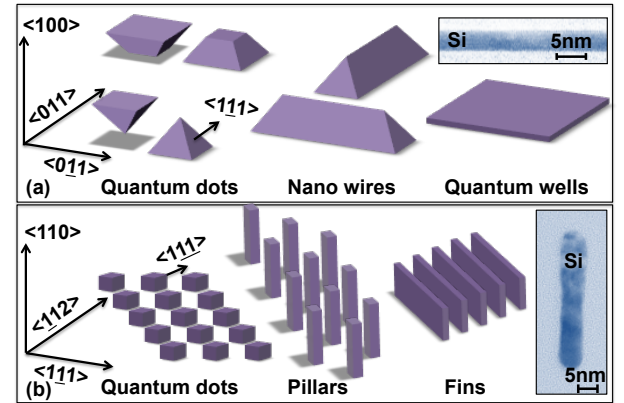

Fig. 2. Challenges for photonic quantum technologies to manipulate single photon. (a) Line edge roughness reduction for low-loss Si waveguides. (b) Wafer scale uniformity of active Si layer controlled by thermal oxidation process. (c) A quantum dot as an artificial atom rather than using random dopants.

Fig. 1. Optical interconnections for long-distance and short-reach applications. III-V materials and LiNbO₃ are dominated for long-distance optical communications, for which the performance is more important than the power consumption. Si photonics is useful for short-reach communications for data centres. For example, C-form-factor pluggable 100-Gigabit-ethernet (CFP100GE) in multi-source agreement (MSA) at the 1310-nm wavelength would be useful. Even for shorter distance applications like intra-board, chip-to-chip, and intra-chip applications for the future, there is no standard nor MSA at this moment, such that alternative wavelengths like 1550nm might be used. The demands for the low power consumption and low cost would be more stringent for shorter distance applications, because the real competitors for optical interconnections are simple copper wirings.

Fig. 3. Nanoscale LEGO®-like building blocks of Si defined by (111) surfaces. (a) Building blocks defined by slanted interfaces using a (100) Silicon-On-Insulator (SOI) substrate. (b) Building blocks defined by vertical sidewall using a (110) SOI substrate.

The record-low propagation loss of 0.4 dB/cm in a Si wire waveguide was achieved by using an advanced fabrication line for 300mm wafer scale.[29] The loss value of ∼ 1 dB/cm in a Si photonic single-mode waveguide is routinely achievable in a commercial line,[30] which is low enough for transceiver applications. However, this value is orders of magnitude higher than that of an optical fibre, ∼ 1 dB/(10km), such that the loss could be even lower by reducing the scattering sources. For future applications in quantum technologies,[21–25] for example, the ultimate requirement is to generate, transmit, and manipulate single photon towards entanglements[31,32] and complicated quantum operations. Then, we cannot tolerate any Line-Edge-Roughness (LER), non-uniformity, or random dopants (Fig. 2) to prevent any loss of entangled photon. In order to achieve this goal, unprecedented levels of process controls are required, which will also useful for the more practical applications in transceiver and sensors.

Here, we describe our ideas to rely on symmetries[1–3,33–37] of Si in order to reduce the propagation loss[38–40] and to apply for optical modulators[41–44] and quantum technologies.[45–48] These days, single crystalline Si wafers with high purity grades exceeding 99.999999999% (eleven 9) are widely available, and we thought it is useful to align nearly perfect crystalline structure to reduce the LER, which was ultimately determined by the size of a resist molecule.[49] It is well known that the anisotropic wet etching is self-limited after defining Si (111) surfaces.[38,50] The idea, here, is to choose a bespoke crystallographic orientation (Fig. 3) to allow the vertical sidewall suitable for various applications.[38–48] Available features of wet-etched structures are limited due to the definition of the crystal surfaces, however, by combining these building blocks and the conventional dry-etched structures with arbitrary curvatures, we can construct various functional devices. Therefore, our idea is similar to LEGO® blocks for nanoscale building blocks. We reported that the propagation loss of Si wire waveguide was ∼ 1 dB/cm, which was remarkably lower than the controlled dry-etched sample in our university line,[38] leading to the developments of novel slot waveguides

and optical modulators.

The outline of this paper is as follows. In the next section 2, we explain our SOI wafer specifications and the fabrication process. The waveguide characteristics are also reviewed. In the section 3, we discuss applications of our slot waveguides in optical modulators. In the section 4, we also discuss our new theoretical design of Si/LiNbO$_3$ hybrid optical modulators in some detail, because this modulator can potentially achieve almost zero power consumption due to the removal of 50-Ω termination. In the section 5, we show the photonic crystal waveguides with broken symmetries, and the possibility of photonic organic chemistry is discussed. In the section 6, we conclude and discuss the future outlook.

2. Symmetries of crystals for Si photonic waveguides

### 2.1 Silicon-On-Insulator wafer specifications

We have asked a global wafer supplier to fabricate bespoke SOI wafers for our Si photonic waveguides (Fig. 4). If we use a standard SOI wafer with the top SOI layer of Si (001), the slanted surface was expected after alkali-wet etching (Fig. 4 (a)). The angle θ of the surface of (111) from the horizontal surface is calculated to be $\theta = \cos^{-1}\left((0, 0, 1) \cdot (1, 1, 1)/\sqrt{3}\right) = \cos^{-1}(1/\sqrt{3}) \approx 54.7°$.[38,50] On the other hand, the bespoke SOI wafer with the Si (110) top surface[38,50] could be patterned vertically to form Si (111) surfaces (Fig. 4 (b)), because the inner product is zero, $(1, -1, 0) \cdot (1, 1, 1) = 0$, where $(1, 1, 0)$ and $(1, -1, 0)$ are equivalent in Si due to the cubic symmetry of a diamond structure.[3] In order to fabricate the vertical sidewall of Si (111), it is important to align the trench along $< 11\underline{2} >$ direction, for which we expect the interface is normal to the substrate, as confirmed by $(1, 1, -2) \cdot (1, -1, 0) = 0$. Therefore, the propagation direction of the Si wire waveguide with the Si (111) wall should be aligned to $< 11\underline{2} >$.[38]
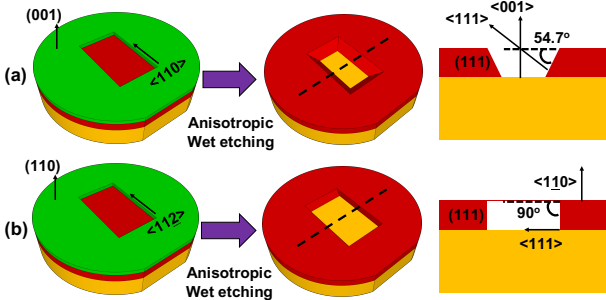

Fig. 4. Silicon-On-Insulator (SOI) substrates. The oxide hard mask (shown in green) was used for alkali wet-etching. The cross sections along the dotted lines show atomically-flat Si (111) interfaces (red) on top of the buried oxide (BOX, orange). (a) Standard SOI wafer with Si (001) layer. (b) Bespoke SOI wafer with Si (110) layer. The flat is aligned along the $< 111 >$ direction for 6-inch wafers. The notch is aligned along the $< 11\underline{2} >$ direction for 8-inch wafers. The alkali wet-etched Si (111) surface is perpendicular to the substrate.

There exists 2 different directions to allow fabrication of Si wire waveguides with Si (111) sidewalls, i.e., $< 11\underline{2} >$ and $< \underline{1}1\underline{2} >$, whose angle in-between is $\cos^{-1}((1, 1, -2) \cdot (-1, -1, -2)/6) = \cos^{-1}(1/3) \approx 70.5°$ (Fig. 5). Regardless of the limited number of building blocks (Fig. 3) by wet-etching, we can consider a lot of variations of designs

(Fig. 5).
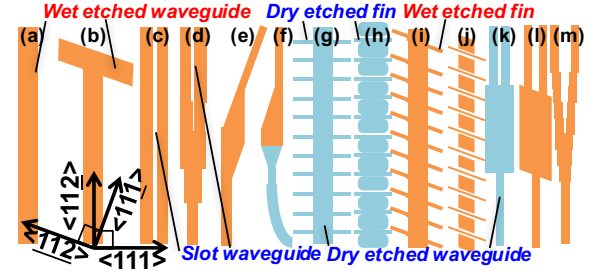
Fig. 5. Variations of Si wire waveguides designs for wet-etching (orange) and dry-etching (blue) on (110) SOI wafers. (a) Wire waveguide with the Si (111) sidewall. (b) Wire waveguides along $< 11\underline{2} >$ and $< \underline{1}1\underline{2} >$. (c) Slot waveguide. (d) Coupler to a slot waveguides. (e) Coupler to straight waveguides with different propagation directions. (f) Coupler between dry and wet etched waveguides. (g) Dry-etched fin waveguide. (h) Dry-etched sub-wavelength array waveguide with fins. (i) Wet-etched fin waveguide. (j) Wet-etched sub-wavelength array waveguide with fins. (k) Dry-etched Multi-Mode-Interference (MMI) splitter. (l) Wet-etched MMI splitter. (m) Wet-etched Y-splitter.
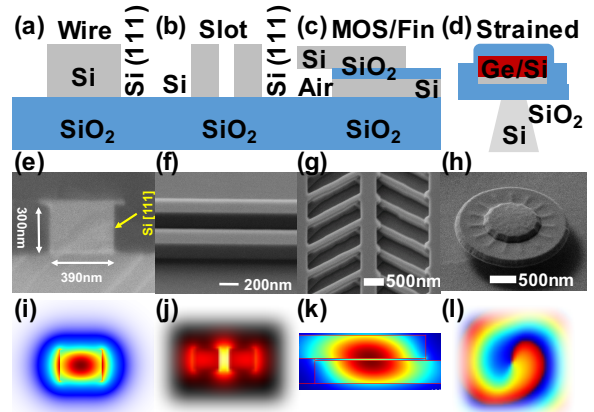
Fig. 6. Novel Si photonic waveguides fabricated in our platform. Schematic structures of (a) a wire waveguide, (b) a vertical slot waveguide, (c) a fin waveguide with a horizontal slot, and (d) a strained Ge microdisk with a grating gear. The corresponding Scanning-Electron-Microscope (SEM) images are shown in (e)-(h), and the simulated mode profiles are shown in (i)-(l), respectively.

2.2 Novel Si photonic waveguides

By using our platform by using anisotropic wet-etching of Si (110) SOI wafers, we fabricated various structures, as shown in Fig. 6.[38–48,51–55] The most standard waveguide is a simple wire waveguide (Figs. 6 (a), (e) and (i)). The original thickness of the SOI layer was 340nm, and it was thinned down to 300nm by thermal oxidation to make a hard mask of SiO$_2$. As an alkali-solution, we used Tetra-Methyl-Ammonium-Hydroxide (TMAH),[38] which is known as a developer of a resist, rather than KOH to prevent alkali-metal contaminations, which is detrimental for an optical modulator due to the high diffusion constant.[1] We have applied more than 1500 % worth for over etching, which corresponds to etch 300nm × 16 = 4.8 μm of

Table II. Comparisons of various efforts to reduce the propagation loss of the Si photonic slot waveguides. F is the confinement factor of the slot modes.

Structure	TiO$_2$ coated	Slab loaded	Asymmetric	Wet-etched
Mode	Centred	Centred	Right-shifted	Centerd
F	21.6 %	8.2 %	6.4 %	21.6 %
Loss	7.0 dB/cm	6.5 dB/cm	2.0 dB/cm	3.7 dB/cm
Reference	[56]	[57]	[58]	[39]

Si along the $< 1\underline{1}0 >$ direction. Nevertheless, the observed side etch was less than 30 nm (as vaguely seen as a hat shape of the SiO$_2$ hard mask in Fig. 6 (e)), which corresponds to an excellent selectivity, exceeding 150:1 between (110) and (111) surfaces.[38] We could increase the selectivity, if required, by changing temperature and adding surfactant.

The propagation losses of the wet-etched waveguides were 0.85dB/cm and 1.08dB/cm for Transverse-Electric (TE) modes and Transverse-Magnetic (TM) modes, respectively, while the corresponding dry-etched ones were 4.70 dB/cm and 1.67 dB/cm.[38] The improvement was especially significant for the TE mode, because the scattering due to LER was more prominent for the TE mode due to the enhanced electric fields at the vertical sidewall.

The successful reduction of the propagation loss in a wire waveguide encouraged us to fabricate more complicated structures including a slot waveguide (Figs. 6 (b), (f) and (j)).[38] In a slot mode, the light is confined in air between adjacent sidewalls (Fig. 6 (f)). Due to the sub-wavelength nature of the narrow slot region, the electric field intensity is significantly enhanced, suitable for applications in gas sensing and bio-medial molecular sensors. However, strong scatterings due to LER are expected due to increased field intensity at the interface, therefore the high propagation loss is usually observed in a slot waveguide with a typical value of $\sim$ 10 dB/cm after dry etching.[38] In order to reduce the propagation loss towards the practical sensing applications, a lot of efforts are being made, e.g., TiO$_2$ coating by Atomic-Layer-Chemical-Vapour-Deposition (ALCVD),[56] insertion of the slab layer,[57] and asymmetric design architecture[58] (Table II). These ideas were all effective compared with as-dry-etched slot waveguides. However, some of ideas[56,57] have trade-off between the optical confinement factor, F, and the reduction of propagation loss. On the other hand, we could maximise the confinement, while the loss was sufficiently reduced.[39] The minimum slot width, we could realise was 100 nm. Below the gap width of 100 nm, TMAH solution did not etch sufficiently. For waveguides with arbitrary narrower slot of the order of a few nm (potentially down to 1nm), we established more complicated process for modulator applications,[41,42] which we describe in the next section.

Please note that the mirror symmetry, in other words, the parity symmetry is broken in the SOI with Si (110) surface, as confirmed by Fig. 5 (i), which is asymmetric against the flip-flop exchange between left and right fin arrays. This asymmetry was useful to allow novel patterning of a double SOI bonded wafer[43] to pattern the bottom layer from the top, as shown in Figs. 6 (c), (g), and (k). First, we have manually bonded two (110) SOI wafers with $\sim$ 10-nm-thick thermal oxide face-to-face without any patterning.[43] In wafer bonding, it is important to avoid any particle contaminations, which prevents sufficient adhesion between layers, such that it was ideal to bond before patterning. Then, the challenge was to pattern the bottom SOI layer from the standard top-down lithography technique. In order to achieve it, we have dry-etched 2 SOI layers and oxidised to remove the damaged sidewalls. After removing the oxide sacrificial layer, we have applied anisotropic TMAH etching. This enabled us to make self-limited asymmetric features between bottom and top SOI layers (Figs. 6(c) and (g)). The left side of multi-fin arrays of Fig. 6 (g) are made of the top SOI layer, which is freestanding in air, because the fins in the bottom SOI layer are not aligned to have stable Si (111) sidewalls. On the other hand, the fins on the right side in the top SOI layer do not have stable Si (111), such that it was wet-etched completely, leaving only the fin arrays in the left SOI layer (Fig. 6 (g)). Consequently, the left fins in the bottom SOI layer is free from the possible capacitive coupling to the bottom SOI layer, which is important for MOS-type modulator applications.[43] The central waveguide is always stable during the wet-etching, protected by Si (111) sidewalls. This process enabled us to fabricate asymmetric fin waveguide through just 1 lithography step, which enables us to access electrically to the top and bottom SOI layers, separately through fin arrays.

We have also fabricated a germanium (Ge) microdisk with a grating gear[53] (Figs. 6 (d), (h), and (l)), which is a vertically light-emitting device towards the monolithic integration of light sources on Si photonic platform.[51,52,54,55,59–83] Ge is an indirect band-gap semiconductor, but a lot efforts are being made to convert it to a direct band-gap semiconductor by tensile-strain-engineering.[4,61,82–84] The TMAH etching is useful to make a suspended bridge structure, because TMAH do not etch Ge at all regardless of the etching of Si of the order of 100 μm.[54,55,64–68] In the structure of Fig. 6 (h), the tensile strain was accumulated at the edge of the micro-disk, where the Whispering-Gallery Mode (WGM) is formed.[53] In order to extract vertically, a grating made of the micro-gears was integrated, and the optical mode with orbital-angular-momentum[85–93] was observed (Fig. 6 (l)).[53]

3. Si photonic modulator with a slot waveguide

3.1 Requirement for optical interconnection

Before introducing our Si phtonic modulator, we would like to briefly review the requirement for optical interconnection.[28,94,108] There are many types of optical modulators based on various mechanisms to change the optical output.[108] Due to the absence of the Electro-Optic (EO) effect in Si, we must rely on other effects. The current industrial standard procedure is to rely on the plasma-dispersion effect, which is coming from the change of the absorption coefficient and subsequent change in the effective refractive index due to Kramers-Kronig relationship, derived from causality.[1,3,7,8] The Mach-Zehnder Interferometer (MZI) is usually employed together with carrier injection structures such as a MOS capacitor,[42,98,100] a pn-junction diode,[96,97] and a pin-junction diode.[99] Alternatively, the Electro-Absorption (EA) effects such as Quantum-Confined Stark Effect (QCSE)[101,102,104] and Franz-Keldysh Effect (FKE)[103,105] are also used by integrating Ge Quantum-Well (QW) or epitaxially grown bulk. These EA modulators are expected to be promising for next generations. Alternatively, the resonant cavity structures such

Table III. Comparisons of various Si photonic modulators. We have picked up just typical examples to estimate the energy per bit, required for the data transmission, and we have not aimed to pick up the best modulators, such that this should not be considered as a full benchmark, which is beyond the scope of this paper. We apologise that we could not include most recent state-of-the-art optical modulators, because the aim of these comparisons is to emphasise the importance to take photo-absorption and coupling efficiency into account for the evaluation of the required energy per bit for data transmission. We assumed that the output optical power of 1mW is required for the power budget, and we estimated our best effort basis from the published information. It is important to take the insertion loss to modulators, and the additional power consumption is expected for Electro-Absorption (EA) modulator due to the photocurrent dissipation. Optical absorption and photocurrent dissipation multiplier for the high (low) state are defined as η_{high} (η_{low}) and μ_{high} (μ_{low}), respectively, following the definition of Miller.[94] The launch efficiency, β, is estimated from the loss as, $\beta = |\eta_{high} - \eta_{low}|/(2 + \eta_{high}\mu_{high} + \eta_{low}\mu_{low})$, and the energy magnification factor is $1/\beta$.[94] The power consumption of the temperature control was not included in this estimate. MZI, QCSE, and FKE mean Mach-Zehnder Interferometer, Quantum-Confined Stark Effect, and Franz-Keldysh Effect, respectively. MOS, pn, and pin stand for a Metal-Oxide-Semiconductor capacitive structure, a pn-junction diode, and a pin-junction diode. SOI, VS, poly-Si, and QW mean Silicon-On-Insulator, Virtual-Substrate (thick $Si_{1-x}Ge_x$ layer with graded index, x to relax strain[95]), and Quantum-Well. V_{pp} is the peak-to-peak voltage under the AC operation. V_π is the voltage required to change the phase shift of π.

Mechanism	MZI	MZI	MZI	MZI	MZI	MZI	QCSE	FKE	QCSE	FKE	Disk	Ring
Carrier control	MOS	pn	pn	MOS	pin	MOS	pin	pin	pin	pin	pn	pin
Waveguide	Slot	Ridge	Ridge	Poly-Si/Si	Wire/Fin	Poly-Si/Si	Ridge	Ge	SiGe	Ge	Wire	Wire
Substrate	SOI	SOI	SOI	SOI	SOI	SOI	VS/SOI	SOI	VS	SOI	SOI	SOI
Active material	Si	Si	Si	Poly-Si/Si	Si	Poly-Si/Si	Ge QW	Ge	Ge QW	Ge	Si	Si
Active length [μm]	500	1,350	3,500	480	250	200	10	55	90	50	4	1
Data transmission [Gbps]	25	40	50	20	12.5	15	7	28	-	-	12.5	12.5
3-db band width [GHz]	-	-	-	-	-	-	-	40.7	23	-	15	-
DC bias [V]	3.0	-	5.0	-	0.81	0	4.0	1.4	3.5	4.0	0	0
V_{pp} [V]	6.0	6.0	6.5	1.2	2.3	1.5	1.0	2.8	1.0	3.0	2.0	8.0
DC extinction ratio [dB]	19	8	-	-	23	5	-	6	10	8	-	16
AC extinction ratio [dB]	3.7	6.5	10.0	-	8.0	3.6	3.0	5.9	3.0	-	3.2	9.0
Insertion loss [dB]	5.5	15	15	-	2.4	2.2	15	5.0	3.0	3.7	1.0	1.0
DC power [mW]	0	0	0	0	0.87	0	0	2.2	1.6	0	0	0
AC power [mW]	89	720	845	90	11.3	7.1	0.0053	1.7	2.5	0.03	0.038	4.2
$V_\pi L$ [V·cm]	1.53	11	2.3	0.13	0.29	0.3	-	-	-	-	-	-
Absorption, η_{high}	0.57	0.78	0.90	-	0.84	0.56	0.62	0.92	0.87	0.91	0.52	0.87
Absorption, η_{low}	0	0	0	-	0	0	0.24	0.68	0.74	0.41	0	0
Photocurrent, μ_{high}	0	0	0	0	0	0	5.9	3.5	5.81	8.8	0	0
Photocurrent, μ_{low}	0	0	0	0	0	0	4.7	0	4.65	5.0	0	0
Launch efficiency, β	0.28	0.39	0.45	-	0.42	0.28	0.06	0.05	0.01	0.04	0.26	0.44
$1/\beta$	3.5	2.6	2.2	-	2.4	3.5	17.9	21.8	80.8	24	3.8	2.3
Useful output [mW]	1.0	1.0	1.0	1.0	1.0	1.0	1.0	1.0	1.0	1.0	1.0	1.0
Laser input [mW]	12.5	81.5	70.3	-	4.1	5.9	166.4	26.4	30.7	9.4	4.8	2.9
Modulator input [mW]	3.5	2.6	2.2	-	2.4	3.5	5.3	8.3	15.4	4.0	3.8	2.3
Photocurrent [mW]	0	0	0	-	0	0	12.6	13.4	65.4	20.0	0	0
Modulator power [mW]	89.0	720.0	845.0	-	12.2	7.1	12.6	15.1	67.9	20.1	0.038	4.2
Power (inc. laser) [mW]	101.5	801.5	915.3	-	16.3	12.9	179.0	41.5	98.6	29.4	4.9	7.0
AC energy [fJ/bit]	3,560	4,500	4,225	4,500	226	470	0.75	61	108	25	3	80
Modulator energy [fJ/bit]	3,560	4,500	4,225	4,500	226	470	1,800	540	2,951	16,713	3	332
Energy (inc. laser) [fJ/bit]	4,059	20,037	18,305	-	1,304	863	25,577	1,481	4,285	24,527	390	564
Temperature control	No	No	No	No	No	No	-	Yes	-	-	Yes	Yes
Pre-emphasis used	No	No	No	No	Yes	No	No	No	No	No	No	Yes
Wavelength range [nm]	>200	>200	>200	>200	>200	>200	22	35	21	14	0.1	0.1
Reference	[42]	[96]	[97]	[98]	[99]	[100]	[101, 102]	[103]	[104]	[105]	[106]	[107]

as a disk[106] and a ring[107] are used, which are showing outstanding low power consumption, although the narrow wavelength range forces to use a temperature controller for heating and cooling. Some of these optical modulators are summarised in Table III.

Ultimately, the overall performance of optical modulators are determined by the *total* power consumption for the data transmission.[28,94] Here, it is important to consider various factors, which are not properly included for the evaluation of required energy per bit.[28,94] The most obvious factor is the coupling efficiency to a modulator from a fibre. As we briefly discussed in the introduction, the true competitor of the optical interconnection to introduce is just a copper wiring, and the advantage to compensate the power consumption for EO/OE conversions were the use of the fibre. If the coupling efficiency is not high enough, we cannot introduce optical interconnection.[28] In that sense, VCSEL[109,110] is still very strong alternative solution, because of the high coupling efficiency vertically coupled to a fibre.

Another important factor is to take the additional energy consumption due to the photocurrent dissipation[28] into account for EA modulators.[28] The absorbed photons are converted to photocurrents and Ohmic dissipation is expected under the application of a finite voltage. We have evaluated energy per bit for several modulators following the proposed procedure by Miller,[94] as shown in Table III. In this evaluation, the output optical power of 1mW is assumed. The conventional measure of the power consumption of an optical modulator is AC energy per bit, which is solely coming from the capacitive charging/dis-charging and/or Ohmic dissipation due to carrier injections/depletions. In AC energy per bit, EA modulators and disk/ring modulators are far superior to the more standard MZI modulators. Then, why industries are not introducing these modulators? One of the reason is the missing energy consumption, which is not included in the standard estimation. If we include the photocurrent dissipation for power consumption, which depends on the input power, the energy per bit of an EA modulator is significantly increased. In the evaluation of Table III, the input power is estimated to realise the assumed output power of 1mW. If the output power is larger, the required energy per bit is increased for an EA modulator, while such an increase is not expected for an MZI modulator. Furthermore, if we include the power consumption of a laser, the total energy per bit is increased further. In our estimation, we have not included the additional power consumption for temperature control. Therefore, an MZI modulator is the most energy efficient solution at this moment. Of course, EA and disk/ring-based modulators could be improved, if we could solve these challenges. For the photocurrents, it was proposed to re-use the absorbed power[94] like a solar cell, and then the overall power consumption would be reduced.

3.2　Horizontal Metal-Oxide-Semiconductor (MOS)-type optical modulator

We think that a MOS-based optical modulator is a promising device as a near-term solution for an optical interconnection,[42,98,100] because carriers are blocked at the oxide interface to prevent current flowing. The evolution from depletion/injection-type modulators using *pn*-junction to MOS-type modulators in Si photonics is reminiscent of the bipolar-to-CMOS evolution in the history of electronics.[1,2]

For both electronics and photonics, the continuous demands of reducing the power consumption to manipulates bits are important towards the sustainable developments.

Previous MOS-based Si photonic modulators were based on vertically stacked MOS structures using polycrystalline (poly-) Si[98,100] similar to the CMOS gate stack. In order to reduce coupling and propagation losses, it would be ideal to replace the poly-Si layer to be a single crystal Si.[41–43] It was also important to reduce the step difference between a standard Si wire/ridge waveguide and a phase shifter suitable for a planar integration. Our challenge was to make an arbitrary narrow oxide-slot feature applicable to MOS-type modulators. As we have explained above, the straightforward fabrication of a slot waveguide is limited to the practical air gap down to 100 nm to allow the TMAH solution to penetrate. Moreover, it is not easy to fill in the air gap uniformly by an oxide, because the volume expansion of the factor of 2 is expected if we oxidise Si to form SiO_2. The coating of Spin-On-Glass (SOG) would be an alternative way, but the quality of SOG would not be suitable for active MOS-based device, for which the high quality oxide is inevitable, even after the thermal annealing.
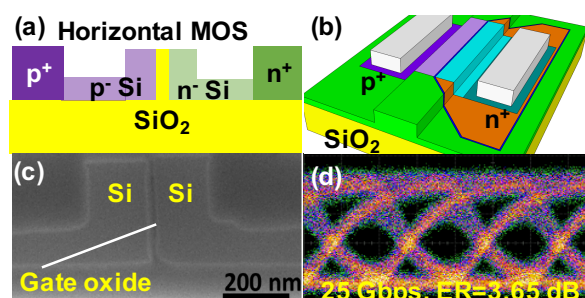
Fig. 7. Si photonic modulator with a horizontal MOS structure. (a) Cross-sectional view. (b) Bird's view. (c) Scanning-Electron-Microscope image. (d) Open eye diagram for 25 Gbps data transmission with the Extinction-Ratio (ER) of 3.65 dB.

The idea is based on the recent development of CMOS electronics. These days, the most of advanced CMOS is based on FinFETs, in which a vertical sidewall of dry-etched interface of Si is used as a channel for CMOS FETs.[111] We cannot tolerate LER of dry-etched interface, such that we have applied anisotropic wet-etching after the dry-etching.[41,42] Subsequently, we have deposited amorphous Si with a connection of the remaining SOI layer as a seed to re-growth the crystal Si after annealing. The Chemical-Mechanical-Polishing (CMP) process was also employed to planarise the surface. This enabled us to fabricate a vertical slot waveguide with the oxide thickness of the order of 10 nm,[41,42] and the scaling down to 1 nm is possible as already realised in FinFETs.[111]

The performance of our Si MOS-type modulator (Fig. 7) with a vertical slot waveguide is summarised in the first column of Table III. We confirmed an open eye diagram at the data transmission of 25 Gbps with the Extinction Ratio (ER) of 3.65 dB (Fig. 7). We used the 14-nm-thick thermal oxide, because the uniformity of our furnace is not good enough to make extremely-thin thermal oxide. Consequently, we needed to apply the relatively large peak-to-peak voltage V_{pp} of 6V, and the energy per bit is still one order of magnitude larger

than that of the state-of-the-art devices.[98–100] Nevertheless, it will be straightforward to scale the oxide thickness down to 2 nm even without introducing high-k gate stacks[2] in an industrial fabrication line.

4. Si/LiNbO$_3$ hybrid modulators towards zero power consumption

Conventional LiNbO$_3$ optical modulators employ a large electro-optic (EO) effect of LiNbO$_3$[27] (without using carrier injection like that in Si photonic modulators[8,108]), enabling high-speed operation at 100 Gbit/s and above. The optical-loss is also low, because of no free-carrier absorption. In addition, they have long-term operational reliability, particularly against heat in comparison with modulators using such organic materials as organic polymers.[112,113] But the drawback is that small LiNbO$_3$ modulators are not easily fabricated because of difficulty in LiNbO$_3$-microstructure patterning, for example, by dry-etching[114] (except for thin LiNbO$_3$-film patterning[115]). Thus the LiNbO$_3$ modulators have a large feature size as large as a few microns in waveguide cross-section size, a few centimeters in length, large power consumption due to transmission-line design with a 50-Ω load, and poor integration with other devices such as Si devices on Si chips.

On the other hand, Si photonic modulators are going to be used as laser modulators for short-reach transceivers in data centers[116] in place of the LiNbO$_3$ modulators (that are still dominant in long-distance optical communications, Fig. 1). Although the Si modulators have advantages of availability of low-cost foundry fabrication processes, of integration capability with various Si photonic devices, and of low-power consumption, they have disadvantages of limited operation speed (typically up to 40-50 Gbit/s), because of useless EO effect due to crystal centrosymmetry.

In this section, combining large-EO-effect LiNbO$_3$ with a compact Si slot waveguide[39,44] (thus forming a Si/LiNbO$_3$-hybrid EO modulator, as illustrated in Fig. 8), we review our theoretical designs of hybrid modulators,[44] which have a small driving voltage and a short device length simultaneously with the help of a very large electric field generated in the slot waveguide.

A recently-developed Si/LiNbO$_3$-hybrid EO modulator with a standard Si waveguide having metal electrodes[117] provided very good performances of modulation speed > 100 Gbit/s and $V_\pi L = 2.2$ V·cm, where V_π is the half-wave voltage and L is the phase shifter length; our Si/LiNbO$_3$-hybrid modulator using the doped slot waveguide shows that $V_\pi L$ is further reduced by a factor of ~ 1/50 compared with that modulator; the details will be described below.

In the next subsection (4.1), we show the methods of fabricating our proposed modulator, and describe its function. In 4.2, we provide our simulation results, and discuss field characteristics realised in the modulator. In 4.3, we present an application of the proposed modulators to high-performance data-transmission modulation (e.g., quadrature amplitude modulation). The summary of Si/LiNbO$_3$-hybrid EO modulator is given in 4.4.

4.1 Device fabrication and function

After preparation of a SOI wafer with the top Si layer p-doped with B or Ga (see Fig. 9(a)), the slot waveguide is fabricated by dry-etching the top Si layer (see Fig. 9(b)), where doping
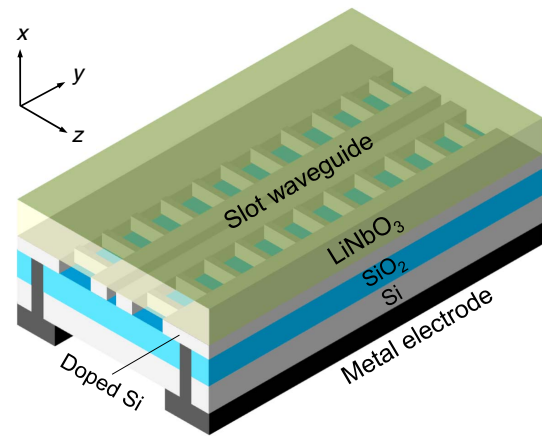
Fig. 8. Si/LiNbO$_3$-hybrid electro-optic modulator. The slot waveguide made of doped-Si is sandwiched between LiNbO$_3$ and SiO$_2$ layers in the vertical (x) direction. The slot waveguide is connected to doped-Si side layers through doped-Si fin-type bridges, where metal electrodes touch the doped-Si side layers.

realises a hole density of ~ 10^{18} cm^{-3}. Due to this doping, the fabricated slot waveguide works as electrodes that apply high voltage to a LiNbO$_3$ layer bonded on the slot waveguide. Note that the hole density is comparable to that in Si photonic modulators but that in our modulator, a large portion of light leaks to the LiNbO$_3$ layer with a very small optical loss of 0.03 dB/cm,[118] which can decrease the big loss of 2.5 cm^{-1} in the doped-Si layer.
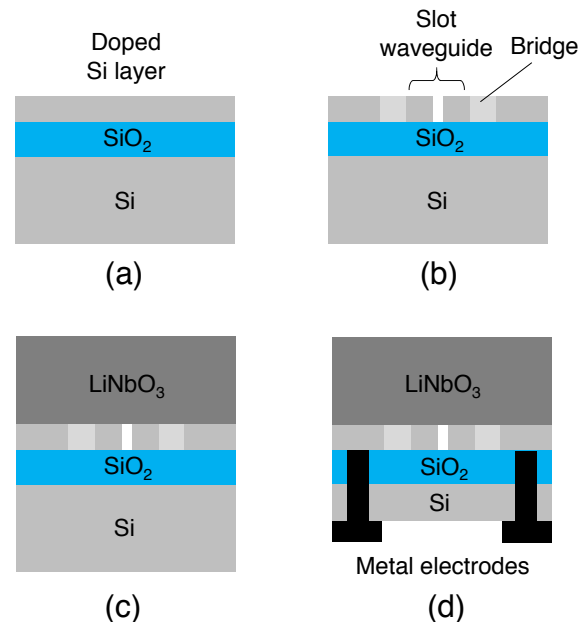
Fig. 9. Fabrication processes of the Si/LiNbO$_3$-hybrid EO modulator. (a) SOI wafer with the top Si layer p-doped. (b) Fabrication of a slot waveguide, fin-type bridges, and side layers at the top Si layer. (c) Direct wafer bonding of LiNbO$_3$ on the patterned Si layer. (d) Formation of metal electrodes through the SiO$_2$ and Si layers.

In the horizontal (z) direction, the slot waveguide is connected to doped-Si side layers through doped-Si fin-type bridges; these side layers and fins are simultaneously produced with the slot-waveguide fabrication. These structures are eas-

ily fabricated by highly-developed Si-foundry processes. As shown below, since a high electric field on the order of 10^7 V/m is present at the slot gap, surface oxidization of the slot waveguide (in an O_2 atmosphere at a high temperature) is necessary, which is effective in preventing electric breakdown; only a few-nm-deep oxidization works well because of its very high breakdown-resistant field $\sim 10^9$ V/m (for < 10-nm-thick SiO_2 layer).[119, 120]

An 'x-cut' LiNbO$_3$ wafer (that has the largest EO coefficient r_{33} in the z-direction for TE beams) is bonded to the patterned doped-Si layer containing the slot waveguide, fins, and side layers by direct wafer-bonding[121] (see Fig. 9(c)). After protection of the topmost LiNbO$_3$ surface (of the LiNbO$_3$/Si/SiO$_2$/Si wafer) with a photoresist, the lower Si substrate is thinned with a solvent and with polishing so that metal electrodes can easily penetrate the SiO$_2$ and Si layers. Metal electrodes are then formed, which touch the doped-Si side layers through holes made with a mask designed for this utilizing a both-sided mask aligner (see Fig. 9(d)). By the above procedures, difficult microstructure-patterning of LiNbO$_3$ can be avoided perfectly.

If the height of the slot waveguide is reduced (e.g., < 300 nm) to be small enough for confined light to leak but not 'radiate' to the LiNbO$_3$ layer, the EO effect of LiNbO$_3$ can be used effectively; such a leaky mode to the LiNbO$_3$ layer is known as an evanescent mode[122] that is actually localised near the Si/LiNbO$_3$ interface, which has a small mode field utilizing confinement effect with the Si slot waveguide. Furthermore, since the doped-Si slot waveguide works as electrodes with close tips, a high electric field is generated between them and goes to the LiNbO$_3$ layer.

The above modulator structure makes it possible to downsize a few-centimetre-long LiNbO$_3$ modulator with a core size of r = 3 - 10 μm to a 0.4-mm-long modulator with r < 1 μm; this also achieves low-power consumption because of allowing use of lumped-constant circuits in place of transmission-line electrodes with 50 Ω. In addition, we will show that reducing the driving voltage to < 1 V (i.e., CMOS-driver-operational voltage) is achieved by this downsizing, as will be shown below.

In 4.2, we show that the proposed modulator can much reduce $V_\pi L$ of the conventional LiNbO$_3$ modulator ($V_\pi L \approx 10$ V·cm[123]) or that of the recently-advanced hybrid modulator ($V_\pi L \approx 2.2$ V·cm[117]); the details of optical and electric fields to obtain the small $V_\pi L$ are also shown in the next section.

4.2 Simulation results and discussion

Figure 10 shows the slot height (h) dependence of optical evanescent mode field $\Phi(x, z)$ at the slot waveguide (sandwiched between LiNbO$_3$ and SiO$_2$) for the waveguide width (d) of 300 nm and the slot gap-size (s) of 50 nm. Those fields were obtained via full-vectorial eigenmode analysis,[124] where the fins in Fig. 8 were replaced with a low refractive-index uniform medium because, if the period of the fins is larger than the input-wavelength size, the fins give almost no influence on the evanescent mode. Here, the device temperature was set at room temperature.[125–127]

As the slot height h decreases, as displayed from Figs. 10 (a)-(c), the mode $\Phi(x, z)$ turns to a perfect radiation mode to LiNbO$_3$, particularly at $h \leq 140$ nm; thus we take h = 200 nm for no leaky operations (for 1.55 μm with TE modes).
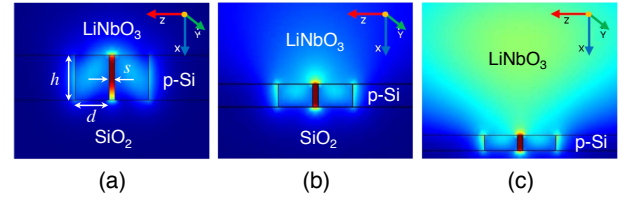
Fig. 10. Optical field $\Phi(x, z)$ of the doped-Si slot waveguide and LiNbO$_3$ at an input wavelength of 1550 nm with TE modes for different slot heights: (a) h = 400 nm, (b) h = 200 nm, (c) h = 140 nm, where the waveguide width d is 300 nm and the slot gap-size s is 50 nm. The colors (blue, yellow, red) of the field strength represent 0, 80, 140 V/m, respectively.
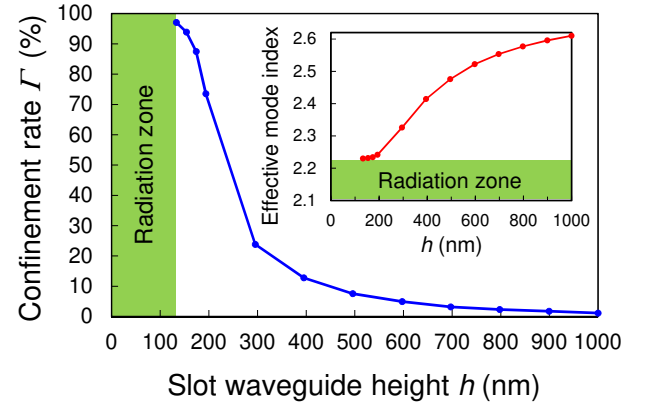
Fig. 11. Slot height (h) dependence of the confinement rate Γ of the optical evanescent mode field in LiNbO$_3$, indicated by the blue curve. The inset, indicated by the red curve, shows the effective mode index for the optical mode field, where 2.21 is the refractive index of LiNbO$_3$ at 1.55 μm for the TE modes. The green zone indicates that the modes are all radiative.

Figure 11 shows the h-dependence of the confinement rate Γ of the mode field in LiNbO$_3$, where Γ is defined by

$$\Gamma = \frac{\iint_{\text{LiNbO}_3} |\Phi(x, z)|^2 \, dx dz}{\iint_{\text{total}} |\Phi(x, z)|^2 \, dx dz}. \tag{1}$$

Here, the denominator of the right-hand side of Eq. (1) is the whole mode field area integration and the numerator is the mode field area integration in LiNbO$_3$. Γ at h = 200 nm is 68%. The inset of Fig. 11 depicts the effective mode index for the optical mode field, where the effective index (2.24) at h = 200 nm for 1.55 μm is still 1.35-% higher than the pristine LiNbO$_3$ refractive index (2.21); thus the optical confinement for waveguiding is maintained.

Figure 12 shows the slot gap-size (s) dependence of the confinement rate Γ at d = 300 nm and h = 200 nm. From Fig. 12, we can see that as s decreases, an optical leakage to LiNbO$_3$ decreases, where Γ decreases almost linearly with s. The inset of Fig. 12 gives the s-dependence of the effective mode index, which shows that as s decreases, the effective mode index becomes large because of tighter light confinement in the slot waveguide with refractive index 3.5 (albeit including air).

Figure 13 displays the calculated cross-sectional (x-z) electric field $E_z(x, z)$[128] (not the optical field) produced from the slot gap for different gap sizes (s); the voltage V_{app} applied to the gap was set at 5 V to obtain a good graphical contrast, but this can be decreased to 1V, as shown in Fig. 14; in this case, the electric-field pattern is almost unchanged, except for its
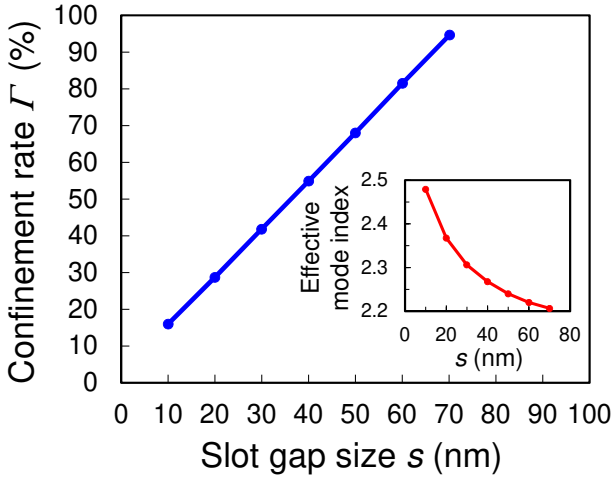
Fig. 12. Slot gap size (s) dependence for the confinement rate Γ in LiNbO$_3$ with $d = 300$ nm and $h = 200$ nm, indicated by the blue curve. The inset, indicated by the red curve, shows the effective index of the mode.
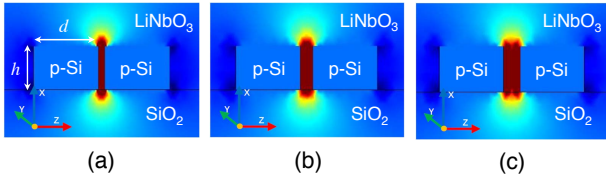
Fig. 13. Electric field $E_z(x, z)$ for the slot waveguide sandwiched between LiNbO$_3$ and SiO$_2$ with different slot gap-sizes: (a) $s = 30$ nm, (b) $s = 60$ nm, (c) $s = 80$ nm. The colours (blue, yellow, red) of the field strength represent 0, 2, 5×10^7 V/m, respectively.
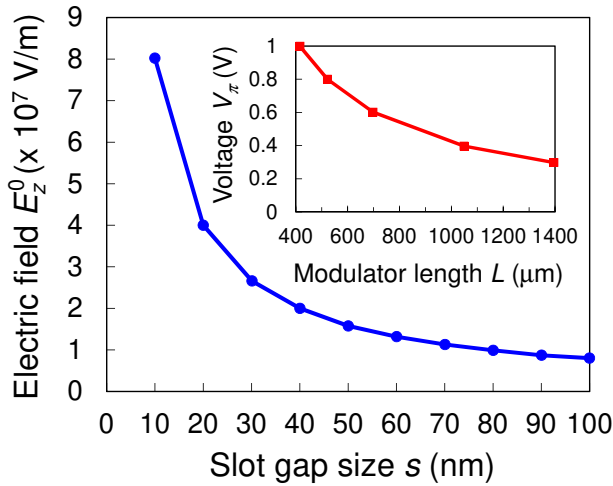
Fig. 14. Slot gap size (s) dependence of the electric field (E_z^0) at LiNbO$_3$ on the slot gap, indicated by the blue curve, when $V_{app} = 1$ V. The inset, indicated by the red curve, shows the modulator length (L) dependence of the half-wave voltage V_π less than 1 V (i.e., CMOS-operational voltage).

amplitude.

As s decreases, the electric field E_z^0 at LiNbO$_3$ on the slot gap becomes large; the s-dependence of E_z^0 is plotted in Fig. 14, when $V_{app} = 1$ V. Here, we observe that E_z^0 increases almost *inversely* with s. But, as given in Fig. 12, the mode field in LiNbO$_3$ becomes small as s decreases; thus there is an optimum s value that gives maximum overlap between the

optical and electric fields. For a device with a small gap size of $s = 50$ nm, the capacitance C is large, such that the CR time constant is also large. This could be overcome by implementing the design of the increased doping concentration of Si electrodes connected to the slotwaveguide for decreasing the resistance R, as demonstrated in an organic-Si hybrid modulator, thus achieving $\sim$ 100-GHz electrical modulation with an optical loss comparable to it.[129] We then plotted the modulator length (L) dependence of the half-wave voltage V_π for < 1 V at $s = 50$ nm in the inset of Fig. 14 (where the free-carrier optical loss in the doped-Si slot waveguide was included). We can see that L is 416 μm for a 1-V application; fortunately this $s = 50$ nm also gives the maximum transmittance T when a Mach-Zehnder (MZ) interferometer of push-pull type, as will be seen in Fig. 15(b), is built; here, T is defined by $T = \Gamma|(e^{-i\phi} + e^{i\phi})/2|^2$ with $\phi = (\pi L/\lambda)n_{\text{eff}}^3\gamma E_z^{\text{eff}}$, where Γ is the same one as given in Eq. (1), λ is the input wavelength or 1.55 μm, n_{eff} is the effective mode index that varies with s, γ is the EO coefficient of LiNbO$_3$ or $\sim$ 30 pm/V,[27] and E_z^{eff} is the averaged electric field where the optical field is present in the EO material.

The inset of Fig. 14 shows that $V_\pi L$ is 4.16×10^{-2} V·cm,[44] which is about 1/240 smaller than that of the conventional LiNbO$_3$ modulators and about 1/50 smaller than that of the aforementioned advanced Si/LiNbO$_3$ modulator. This is due to a small-sized gap in our slot waveguide that works as close-tip electrodes. In comparison with the previously reported modulators, we confirmed the usefulness of the doped-Si slot waveguide in our hybrid modulator to obtain a small $V_\pi L$; the small modulator length ($L = 416$ μm) is also advantageous in avoiding the use of transmission lines of 50 Ω that causes large electrical-power consumption, as mentioned in the previous section.

4.3 Application of proposed modulators

In this final section, we show a device design for an application of the proposed modulators to an optical large-data transmitter using 16 quadrature amplitude modulation (QAM); the design is given in Figs. 15(a)-(c). (The extension to 2^N QAM ($N > 4$) is easily made.) Here, propagating waves are set to be TE modes.

In Fig. 15(a), at the first Y junction at the left, an input wave of frequency ω coming from an outside laser diode is divided into two waves. Let the wave at A be described by $E \cos(\omega t)$, where E is its field amplitude. The wave at B is $\pi/2$-phase-shifted with the proposed EO modulator working as a phase modulator (PM); this wave is thus described by $E \cos(\omega t + \pi/2) = -E \sin(\omega t)$. The waves, divided at the second Y junction just after A, go in Mach-Zehnder intensity modulators MZ1 and MZ2 (each of which is constructed of two PMs) for intensity modulation. These can generate four types of optical signals: (0, 0), (0, 1), (1, 0), (1, 1) for (MZ1, MZ2), respectively. Applied-voltage adjustments of MZ1 and MZ2 can also adjust signal amplitude F and $F/2$ at MZ1 and MZ2, respectively. Owing to these amplitude adjustments, even though those signals are combined at C, the four-type signals are distinguishable, because the combined wave using (0, 0), (0, 1), (1, 0) or (1, 1) gives an amplitude of 0, $F/2$, F or $3F/2$, respectively; hereafter, these amplitudes are denoted by I_i (i = 1 - 4).

In the same way, MZ1' and MZ2' in Fig. 16(a) can give
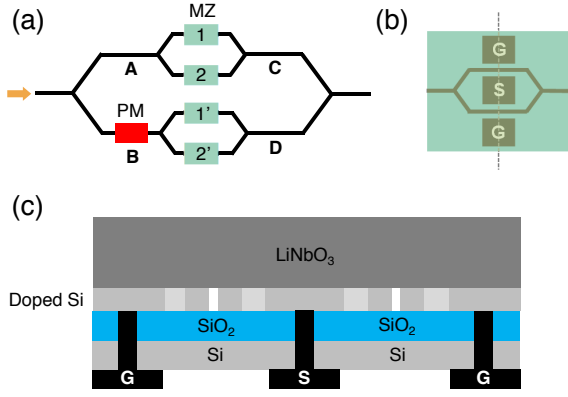
Fig. 15. (a) Device design for 16 QAM. A phase modulator (PM) gives a $\pi/2$-shift to the wave passing through it. Mach-Zehnder intensity modulators (MZ) create 0/1 optical signals by applying electrical voltages; the amplitude of this '1' signal can be adjusted by applied-voltage control. (b) Detail of MZ. G and S are ground and signal electrodes, respectively. (c) Cross-section of MZ when MZ is cut through the dashed line in (b), where the black thick lines are metal electrodes.

signal amplitude F and $F/2$ at MZ1' and MZ2', respectively. The same four-type signals (but with the $\pi/2$-shifted phase) can be clearly recognised even after they are combined at D; hereafter, these combined amplitudes are represented by Q_j (j = 1 - 4).

The waves with those amplitudes I_i and Q_j can easily be distinguished even after they are combined with the final Y junction at the right in Fig. 15(a), because the combined waves are composed of different amplitudes $\sqrt{I_i^2 + Q_j^2}$ and different phases θ_{ij} for different i and j, as given by

$$
\begin{aligned}
E_{\text{output}} &= I_i \cos(\omega t) - Q_j \sin(\omega t) \\
&= \sqrt{I_i^2 + Q_j^2} \cos(\omega t + \theta_{ij}), \qquad (2)
\end{aligned}
$$

where $\theta_{ij} = \arctan(Q_j/I_i)$. In this way, a transmitter with 16 QAM can easily be built with our proposed modulators. Its signal demultiplexing can be performed by an ordinary homodyne-detection scheme.[130] The proposed integrated-device design realises such expanded-data-transmission modulation as 16 QAM on a small Si chip just by setting LiNbO$_3$ on it.

4.4 Summary of Si/LiNbO$_3$-hybrid modulator

We have analysed the optical and electrical properties of our efficient Si/LiNbO$_3$-hybrid EO modulator with a doped-Si slot waveguide, where the doped-slot waveguide works as narrow-gapped electrodes to provide a large electric field and a small $V_\pi L$. By gradually reducing the slot height, we have clarified that there is a threshold height between optically-evanescent and perfectly-radiative modes; we have used a slot height that maintains the evanescent mode for the modulator design. Having obtained an optimised slot-gap size for the best EO modulation, we have theoretically shown a less-than-1/100 reduction of $V_\pi L$ from that of conventional LiNbO$_3$ modulators and a $\sim$ 1/50 reduction of $V_\pi L$ from that of the recently-advanced Si/LiNbO$_3$ modulator containing a standard Si waveguide. Furthermore, using the proposed modulators, we have presented an integrated-device design for such large-data-transmission modulation as 16 QAM.

5. Broken symmetries of photonic crystals

So far, we have discussed our Si photonic waveguides with atomically-flat Si (111) surfaces and applications to optical modulators and sensors using slot waveguides. As shown in Figs. 5 and 6, these waveguides have broken mirror symmetries, because the Si (110) SOI layer is asymmetric between left and right with respect to the < 11$\underline{2}$ > direction. The concept of broken symmetries can also be applied to photonic crystals rather than single crystal of Si. Here, we review our attempts to manipulate symmetries of photonic states propagating in a photonic crystal line-defect waveguides.[45–48]

5.1 Opening of band-gap & emergence of 2-level system by controlling the mismatch

It is well established that opening of the effective band gap is realised in a photonic crystal made of triangular arrays of holes in a free-standing slab of Si.[131,132] The mechanism of the opening of the band-gap is due to its periodicity of the lattice with the lattice constant of a and consequent Brillouin-zone folding[131] quite similar to the formation of the Bloch state in a conventional material due to the crystal symmetry.[3] By making removing holes in the centre of a photonic crystal, line-defects are formed to allow the in-gap states for the propagation of photons in a photonic crystal waveguide.[131] In a standard design of photonic crystal waveguide, a mirror symmetry with respect to the centre of the waveguide is still maintained as shown in Fig. 16 (a). In the band structure with a mirror symmetry, there is a band crossing away from the edge of the Brillouin-zone, and there is a band degeneracy at the crossing point, which can be described by a two-level system.[45] The existence of the two branches was simply coming from the multi-mode nature of our photonic crystal design by adjusting the width of the waveguide to have modes with even and odd nodes.[45]
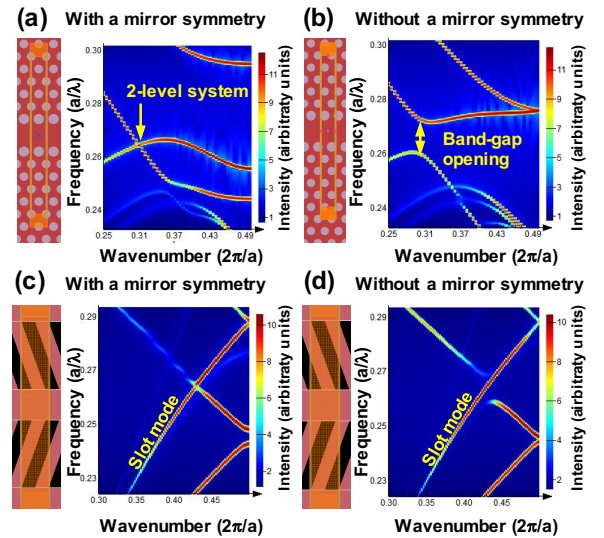
Fig. 16. Impact of symmetries of photonic crystal waveguides on band structures. a is the lattice constant of a photonic crystal, and λ is the wavelength of the propagating photon. We considered triangular lattice (a) with and (b) without a mirror symmetry, and fin-waveguides (c) with and (d) without a mirror symmetry. The shaded orange regions are unit cells used for numerical simulations.

Here, we introduced a mismatch between upper and lower

photonic crystals by introducing the phase-shift between 2 photonic crystals. In analogy with condensed-matter physics, this corresponds to have a dislocation[3] between 2 separated photonic crystals. The photonic crystals have a glide plane symmetry, which is the combination of the mirror reflection and the translation. The mismatch is continuously introduced and it becomes maximum at the maximum mismatch of $a/2$.[45–48] The introduction of this mismatch was considered[36] previously, but, the band crossing point was located within the light cone.[36] In our design, the crossing point was designed to be located outside the light cone, such that this band gap opening was experimentally confirmed.[46]

Let's discuss why the band-gap is opening up? The mechanism of the additional band-gap opening is completely different from the simple periodicity, because the original photonic crystal already has periodicity of a and the introduction of the mismatch cannot change the periodicity. In the original photonic crystal of Fig. 6 (a), we had a mirror symmetry, and in other words, we had a parity symmetry. Assuming the parity operator[31,37,133,134] to be $\mathcal{P}$, and the scalar potential of the electro-magnetic wave to be ψ, which is actually a wave-function of a photon, twice of $\mathcal{P}$ operations bring back to the original state at the crossing point. This means

$$\mathcal{P}^2\psi = \psi, \tag{3}$$

which means the eigenvalue of $\mathcal{P}$ must be

$$\mathcal{P}\psi = \pm\psi. \tag{4}$$

$\mathcal{P} = +1$ corresponds to the parity even mode and $\mathcal{P} = -1$ corresponds to the parity odd mode. These 2 modes constitute the 2-level system.[45] By introducing the mismatch, the symmetry is adiabatically broken, such that these two orthogonal modes are mixing each other to form bonding and anti-bonding modes[45] as for lower energy states.
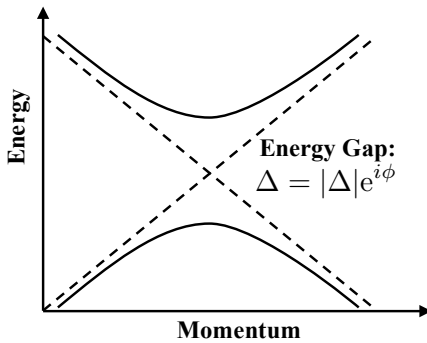
Fig. 17. Quantum mechanical two-level system. The dotted line corresponds to the original states before mixing 2 modes. After the on-set of the hybridisation of 2 systems, the bonding and the anti-bonding states are formed (solid lines) with opening of the band gap. This corresponds to the emergence of the effective mass.

This is a typical behaviour for all quantum mechanical systems, ranging from the Heitler-London theory of H_2 molecule,[3] Bardeen-Cooper-Schrieffer (BCS) theory of superconductivity,[135,136] to Nambu-Anderson-Higgs-Goldstone theory for the emergence of mass[137–140] (Fig. 17). Highlighting the most important aspect of the BCS the-

ory,[3,135,136] the Hamiltonian of the system in a spinor representation,

$$\mathcal{H} = \begin{pmatrix} \epsilon_k & \Delta \\ \Delta^* & -\epsilon_k \end{pmatrix}, \tag{5}$$

becomes diagonalised to be $E^2 = \epsilon_k^2 + |\Delta|^2$ after the formation of the Cooper pair upon the superconducting phase transition. This means that the original linear dispersion, $\epsilon_k = \hbar c k$, becomes quadratic as a function of the wavenumber k. Nambu was inspired by the theory of superconductivity by comparing this dispersion with that of Einstein's theory of relativity, $E^2 = (cp)^2 + (mc^2)^2$, where $p = \hbar k$ is the momentum and m is mass of an elementary particle.[141] Nambu suggested the formation of the energy gap by spontaneous symmetry breaking leads the emergence of the mass of an elementary particle, $|\Delta| = mc^2$, which is now known as Nambu-Higgs mechanism,[138,139] as experimentally confirmed as observing Higgs bosons. The phase degree of freedom, ϕ defined from $\Delta = |\Delta|e^{i\phi}$, also plays a very important role to recover the symmetry as a collective mode.[137–140]

In our case, the symmetry was broken *a priori* as a design of the system, such that the on-set of a phase transition of the vacuum is not required. Nevertheless, the mechanism is essentially the same. The mass of a photon is zero in the vacuum, travelling at the speed of light c (Table I), and in a material, it is still massless with the renormalised velocity of $v = c/n$. However, in our photonic crystal waveguide with a broken mirror symmetry (Fig. 16 (b)), the energy-gap is opening up, leading to the massive dispersion, $m \neq 0$. This character is useful for a slow light,[131] because the velocity of the mode is reduced, substantially due to the emergence of mass.

We can also manipulate symmetries of our waveguides with fins (Figs. 16 (c) and (d)). In this case, the TM slot mode and the TE none-slot mode were mixing, but due to the small overlap between modes, the opening of the band-gap was limited and the slot mode was robust against the introduction of the mismatch.

5.2 Photonic organic chemistry and possible application to quantum simulations

Above analysis suggests that we can manipulate a two-level system by controlling the parity symmetry of photonic crystals. The actual states are more complicated than a simple picture of hybridising modes of even and odd parity states, because we must consider polarisation and orbital states.[45–48]

We start to explain from the nodes as quantum numbers for a photonic crystal waveguide with a mirror symmetry (Fig. 16 (a)). Setting up a coordinate to be (x, y, z), where x is the direction of the propagation, y is the in-plane direction perpendicular to x, and z is the out-of-plane direction perpendicular to the substrate, the photonic crystal waveguide contains an index guided mode, which is dominated by a standard transverse component, E_y, and a photonic-crystal guided mode, which is dominated by longitudinal component, E_x, due to strong reflections by photonic crystals. Both index and photonic-crystal guided modes contain small components for orthogonal directions, such that they are described by number of nodes, as (n, m), where n and m are number of nodes for x and y directions. In our simulation of Fig. 16 (a), the index guided mode is described by $(1, 0)$ and the photonic-crystal guide
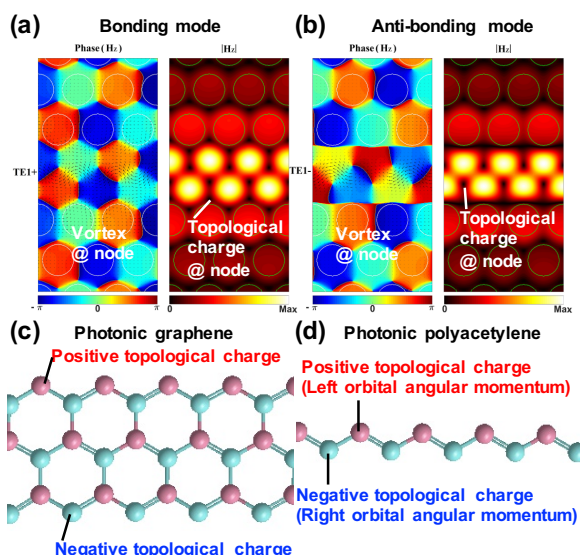
Fig. 18. Photonic organic chemistry realised in Si photonic waveguides with broken parity symmetries. Electro-Magnetic field profiles were obtained by numerical simulations based on a Finite-Difference-Time-Domain (FDTD) method. (a) Photonic graphene of bonding mode found in phase (left) and amplitude (right) of magnetic field. (b) Photonic poly-acetylene of anti-bonding mode found in phase (left) and amplitude (right) of magnetic field. Topological configurations of vortex arrays with alternative topological charge, forming (c) photonic graphene and (d) photonic poly-acetylene states. Positive and negative topological charges correspond to nodes, surrounded by fields with left and right orbital angular momentum, respectively.

mode is described by (2, 1). In this way, we obtained naturally quantised integers to describe modes. However, according to quantum-mechanics, we also expect conjugate quantum valuable, corresponding to a phase, if the integer quantum number is obtained.[31,37,133,134,142–144] What is the conjugate quantum observable to parity? Parity is described by 2 states, $\mathcal{P} = +1$ and $\mathcal{P} = -1$, and therefore, can we identify 2 quantum states for a photon? The hint was found in a fundamental property of a photon (Table I), which has 2 polarisation states. In fact, the 2 modes have orthogonal polarisations, one is dominated by E_x and the other dominated E_y, such that they can form a 2-level system.[45] By introducing the mismatch (Fig. 16 (b)), the parity symmetry is broken, which allows to hybridise these 2 orthogonal states, forming bonding and anti-bonding states with different polarisation states (Fig. 18).[45–48] The phase is, thus, naturally understood as the angles, (θ, ϕ), in the Poincaré sphere using Stokes parameters.[27,45–48,145–148] The polarisation states are observables using various polarimetry techniques.[149,150]

For our photonic crystal with a broken mirror symmetry, it is easier to describe by using magnetic field component along z, H_z, rather than E_x and E_y, because H_z is dominated for both modes (Fig. 17).[45–48] Interestingly, the mode profiles contain periodic arrays of nodes and it is topologically the same structure as graphene for the bonding mode with the lower energy, and it is poly-acetylene for the anti-bonding mode with the higher energy (Fig. 18). At the node, the intensity becomes zero, while the field is circulating surrounding the node. Since the field must be regular analytic function, the field must be described by a single-valued function,

which leads the quantisation of the optical Orbital-Angular-Momentum (OAM).[45–48,85–93] Depending on the direction of the rotation, the left and right OAM are expected. The node is quite often called as topological charge, since it is located at the centre of the vortex of lights. Positive and negative charges correspond to the left and right OAM, respectively. In our case, it might be appropriate to call them as topological monopole, since the magnetic field is circulating. Please note that there is nothing involved, which has the dimension of charge nor monopole. Mathematically, it would be rigorous to describe them as winding numbers. As shown in Fig. 18, positive and negative topological charges are forming photonic organic molecules with alternating configurations similar to an Anti-Ferro (AF) magnet.[3,143,144] Our results suggest that we might be able to simulate various organic molecules using a Si photonic platform. The most energetically favourable configurations would be automatically realised to minimise the energy of photons to travel in a photonic crystal waveguide. There are a lot of attentions in quantum simulations,[21–25] and they will be useful for material optimisations to elucidate the mechanism of complex quantum many-body problems such as high-temperature superconductors[143,144] and ultimately for simulating the process of the early Universe.[151]

6. Conclusion and future vision
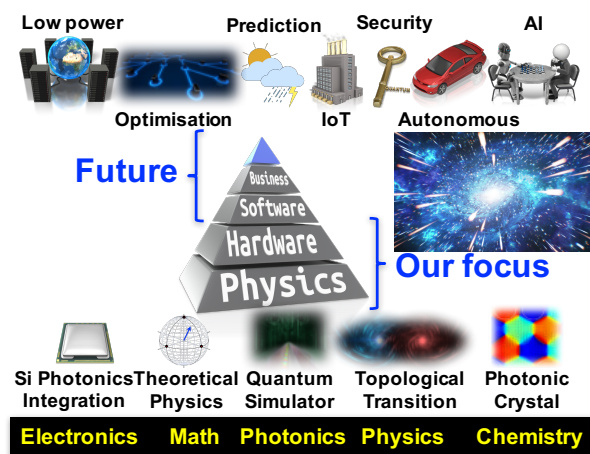
Fig. 19. Future vision of impacts enabled by Si photonics. Low power data transmission in a data centre is already growing significantly and will grow even further for various optimisation problems including AI and IoT networks. LiDAR and biomedical sensing applications are next promising ares for applications of Si photonics. For the future, Si photonics will also enable for quantum technologies and photonics and electronics will be seamlessly synchronised using both classical and quantum nature of photons.

We have reviewed our recent progress on developing Si photonic waveguides with broken symmetries and discussed their applications in low-power optical modulators and quantum technologies.[38–48,51–55] The use of the atomically-flat Si (111) interface severely limits the possible features, we can realise. Nevertheless, by combining these building blocks, we could construct functional devices such as wire-waveguides,[38] slot-waveguides,[39,41] fin-waveguides,[43] grating-couplers,[40] Ge light sources,[51–55] horizontal MOS-type modulators,[41–43] hybrid modulators,[44] and photonic crystals.[45–48] The proposed

MOS-type optical modulators would be a practical near-term solution for an active-optical cable in a data centre[42] (Fig. 19).

Manipulations of symmetries of photonic crystals by breaking the parity symmetry allowed us to open a new band-gap by hybridising modes with different polarisation states.[45–48] The simulated mode profiles show photonic graphene and photonic poly-acetylene structures with vortex arrays of alternating topological charges. In order to develop a quantum simulator using the 2-level system of photons, we need to develop a system with reconfigurable photonic circuits. Si photonics would be an ideal platform to integrate a lot of optical components on a chip for quantum technologies. For quantum applications, it is fundamentally important to address the nature of a photon, because even the most renown physicist, Einstein, confessed that he could not understand what is the light quanta.[152] In particular, it is believed that the spin and orbital angular momentum cannot be good quantum observables, independently, while the sum of these could be well-defined.[153–156] In order to use photons for quantum technologies, it is crucial to revisit this issue and clarify the condition to use quantum degrees of freedom in more detail.

Acknowledgments

1) S. M. Sze and M. K. Lee: *Semiconductor Devices: Physics and Technology* (John Wiley and Sons, 2012) 3rd ed.
2) Y. Taur and T. H. Ning: *Fundamentals of Modern VLSI Devices* (Cambridge University Press, 2013) 2nd ed.
3) C. Kittel: *Introduction to Solid State Physics* (John Wiley & Sons, 2004) 8th ed.
4) Y. Ishikawa and S. Saito: IEICE Electronics Express **11** (2014) 1.
5) G. E. Moore: Electronics **38** (8) (1965) 114.
6) : International Technology Roadmap for Semiconductor (ITRS). URL http://www.itrs.net
7) G. T. Reed and A. P. Knights: *Silicon Photonics* (Wiley, 2004).
8) G. T. Reed: *Silicon Photonics: The State of the Art* (John-Wiley & Sons, NJ, 2008).
9) Y. Arakawa, T. Nakamura and Y. Urino: Communications Magazine, IEEE **51** (3) (2013) 72.
10) Eds. S. Fathpour and B. Jalali: *Silicon Photonics for telecommunications and biomedicine* (CRC Press, 2012).
11) Eds. L. Pavesi and D. J. Lockwood: *Silicon Photonics* (Springer, 2004).
12) Eds. L. Pavesi and G. Guillot: *Optical Interconnects The Silicon Approach* (Springer, 2006).
13) Eds. L. Vivien and L. Pavesi: *Handbook of Silicon Photonics* (Taylor and Francis, 2013).
14) K. Wada, J. Liu, S. Jongthammanurak, D. D. Cannon, D. T. Danielson, D. Ahn, S. Akiyama, M. Popovic, D. R. Lim, K. K. Lee, H. C. Luan, Y. Ishikawa, J. Michel, H. A. Haus and L. C. Kimerling: *Si Microphotonics for Optical Interconnection* (Springer Verlag, Berlin, 2006).
15) H. Zimmermann: *Integrated Silicon Opto-electronics* (Springer, 2000).
16) : *EE Times*: https://www.eetimes.eu/silicon-photonics-reaches-prime-time/ .
17) T. Baba: Proc. 24th Microoptics Conference (MOC, Toyama) (2019) SS2.
18) S. Noda: Proc. 24th Microoptics Conference (MOC, Toyama) (2019)

19) G. Z. Mashanovich, M. Nedelijkovic, J. Soler-Penades, Z. Qu, W. Cao, A. Osman, Y. Wu, C. J. Stirling, Y. Qi, Y. X. Cheng, L. Reid, C. G. Littlejohns, J. K. Z. Zhao, M. Takenaka, T. Li, Z. Zhou, F. Y. Gardes, D. J. Thomson and G. T. Reed: Opt. Mater. Express **8** (2018) 2276.
PL3.
20) T. Baba: Photonics **6** (2019) 65.
21) A. Aspuru-Guzik and P. Walter: Nat. Phys. **8** (2012) 285.
22) J. B. Spring, B. J. Metcalf, P. C. Humphreys, W. S. Kolthammer, X. M. Jin, M. Barbieri, A. Datta, N. Thomas-Peter, N. K. Langford, D. Kundys, J. C. Gates, B. J. Smith, P. G. R. Smith and I. A. Walmsley: Science **339** (2013) 798.
23) G. Masada, K. Miyata, A. Politi, T. Hashimoto, J. L. O'Brien and A. Furusawa: Nat. Photon. **9** (316–319).
24) M. J. Hartmann: J. Opt. **18** (2016) 104005.
25) S. Paesani, A. A. Gentile, R. Santagati, J. Wang, N. Wiebe, D. P. Tew, J. L. O'Brien and M. G. Thompson: Phy. Rev. Lett. **118** (2017) 100503.
26) Y. Tamura, H. Sakuma, K. Morita, M. Suzuki, Y. Yamamoto, K. Shimada, Y. Honma, K. Sohma, T. Fujii and T. Hasegawa: J. Light. Technol. **36** (2018) 44.
27) Y. Yariv and P. Yeh: *Photonics: optical electronics in modern communications* (Oxford University Press, 1997).
28) D. A. B. Miller: Proceedings of the IEEE **97** (7) (2009) 1166.
29) T. Horikawa, D. Shimura, H. Okayama, S. H. Jeong, H. Takahashi, J. Ushida, Y. Sobu, A. Shiina, M. Tokushima, K. Kinoshita and T. Mogami: IEEE J. Selec. Top. Quant. Elec. **24** (2018) 8200415.
30) F. Boeuf, S. Cémer, E. Temporiti, M. Ferè, M. Shaw, C. Baudot, N. Vulliet, T. Pinguet, A. Mekis, G. Masini, H. Petiton, P. L. Maitre, M. Traldi and L. Maggi: J. Light. Technol. **34** (2016) 286.
31) M. Fox: *Quantum Optics: An Introduction* (Oxford University Press, 2006).
32) A. Furusawa and P. v. Loock: *Quantum Teleportation and Entanglement: A Hybrid Approach to Optical Quantum Information Processing* (Wiley-VCH, 2011).
33) S. Coleman: *Aspects of Symmetry* (Cambridge University Press, 1985).
34) Y. T. T. Inui and Y. Onodera: *Group Theory and Its Applications in Physics* (Springer, 1996) 2nd ed.
35) W. Ludwig and C. Falter: *Symmetries in Physics* (Springer-Verlag, 1996).
36) A. Mock, L. Lu and J. O'Brien: Phys. Rev. B **81** (2010) 155115.
37) S. K. Özdemir, S. Rotter, F. Nori and L. Yang: Nat. Mater. **18** (2019) 783.
38) K. Debnath, H. Arimoto, M. K. Husain, A. Prasmusinto, A. Z. Al-Attili, R. Petra, H. M. H. Chong, G. T. Reed and S. Saito: Front. Mater. **3** (2016) 10.
39) K. Debnath, A. Z. Khokhar, S. A. Boden, H. Arimoto, S. Z. Oo, H. M. H. Chong, G. T. Reed and S. Saito: Front. Mater. **3** (2016) 51.
40) A. Prasmusinto, M. Sotto, A. Z. Al-Attili, K. Debnath and S. Saito: Photonics and Nanostructures-Fundamentals and Applications (PNFA) **26** (2017) 1.
41) K. Debnath, A. Z. Khokhar, G. T. Reed and S. Saito: IEEE Photon. Technol. Lett. **29** (2017) 1269.
42) K. Debnath, D. J. Thomson, W. Zhang, A. Z. Khokhar, C. Littlejohns, F. Byers, L. Mastronardi, M. K. Husain, K. Ibukuro, F. Y. Gardes, G. T. Reed and S. Saito: Photon. Res. **6** (2018) 373.
43) J. Byers, K. Debnath, H. Arimoto, M. K. Husain, M. Sotto, Z. Li, F. Liu, K. Ibukuro, A. Khokhar, K. Kiang, S. A. Boden, D. J. Thomson, G. T. Reed and S. Saito: Opt. Exp. **26** (2018) 33180.
44) I. Tomita, K. Debnath, K. Ibukuro, M. K. Husain, J. Byers, Z. Zhang and S. Saito: Proc. the 15th Int. Conf. on Group IV Photonics (GFP, Cancun, Mexico) (2018) WP8.
45) M. Sotto, I. Tomita, K. Debnath and S. Saito: Front. Phys. **6** (2018) 85.
46) M. Sotto, K. Debnath, A. Z. Khokhar, I. Tomita, D. Thomson and S. Saito: J. Opt. Soc. Am. B **35** (2018) 2356.
47) M. Sotto, K. Debnath, I. Tomita and S. Saito: Phys. Rev. A **99** (2019) 053845.
48) S. Saito, M. Sotto, K. Debnath, J. Byers, A. Z. A.-Attili, I. Tomita, D. Burt, M. K. Husain, K. Ibukuro, D. J. Thomson, W. Zhang, B. Chen, F. Y. Gardes, G. T. Reed and H. N. Rutt: Proc. 24th Microoptics Conference (MOC, Toyama) (2019) C5.
49) A. Yamaguchi, H. Fukuda, T. Arai, J. Yamamoto, T. Hirayama, D. Shiono, H. Hada and J. Onodera: Journal of Vacuum Science &

Technology B: Microelectronics and Nanometer Structures Processing, Measurement, and Phenomena **23** (2005) 2711.

50) K. K. Lee, D. R. Lim and L. C. Kimerling: Opt. Lett. **26** (2001) 1888.

51) A. Z. Al-Attili, S. Kako, M. K. Husain, F. Y. Gardes, H. Arimoto, N. Higashitarumizu, S. Iwamoto, Y. Arakawa, Y. Ishikawa and S. Saito: Jpn. J. Appl. Phys. (052101).

52) A. Z. Al-Attili, S. Kako, M. K. Husain, F. Y. Gardes, N. Higashitarumizu, S. Iwamoto, Y. Arakawa, Y. Ishikawa, H. Arimoto, K. Oda, T. Ido and S. Saito: Front. Mat. **2** (2015) 43.

53) A. Z. Al-Attili, D. Burt, Z. Li, N. Higashitarumizu, F. Y. Gardes, K. Oda, Y. Ishikawa and S. Saito: Opt. Exp. **26** (2018) 34675.

54) D. Burt, A. Al-Attili, Z. Li, F. G. nad m. Sotto, N. Higashitarumizu, Y. Ishikawa, K. Oda, O. M. Querin, S. Saito and R. Kelsall: Opt. Exp. **25** (2017) 22911.

55) D. Burt, J. Gonzales, A. Al-Attili, H. Rutt, A. Z. Khokar, K. Oda, F. Gardes and S. Saito: Opt. Exp. **27** (2019) 37846.

56) T. Alasaarela, D. Korn, L. Alloatti, A. Säynätjoki, A. Tervonen, R. Palmer, J. Leuthold, W. Freude and S. Honkanen: Opt. Exp. **19** (2011) 11529.

57) R. Ding, T. Baehr-Jones, W. J. Kim, X. Xiong, R. Bojko, J. M. Fedeli, M. Fournier and M. Hochberg: Opt. Exp. **18** (2010) 25061.

58) A. Spott, T. Baehr-Jones, R. Ding, Y. Liu, R. Bojko, T. O'Malley, A. Pomerene, C. Hill, W. Reinhardt and M. Hochberg: Opt. Exp. **19** (2011) 10950.

59) J. Liu, X. Sun, R. Camacho-Aguilera, L. C. Kimerling and J. Michel: Optics Lett. **35** (5) (2010) 679.

60) R. E. Camacho-Aguilera, Y. Cai, N. Patel, J. T. Bessette, M. Romagnoli, L. C. Kimerling and J. Michel: Opt. Express **20** (10) (2012) 11316.

61) J. Liu, L. C. Kimerling and J. Michel: Semicond Sci. Technol. **27** (2012) 094006.

62) J. Liu: Photonics **1** (2014) 162.

63) Z. Liu, Y. Li, C. He, C. Li, C. Xue, Y. Zuo, B. Cheng and Q. Wang: Appl. Phys. Lett. **104** (2014) 191111.

64) D. Nam, D. Sukhdeo, A. Roy, K. Balram, S. L. Cheng, K. C. Y. Huang, Z. Yuan, M. Brongersma, Y. Nishi, D. Miller and K. Saraswat: Opt. Express **19** (2011) 25866.

65) D. Nam, D. Sukhdeo, S. L. Cheng, A. Roy, K. C. Y. Huang, M. Brongersma, Y. Nishi and K. Saraswat: Appl. Phys. Lett. **100** (2012) 131112.

66) D. Nama, D. S. Sukhdeo, J.-H. Kang, J. Petykiewicz, J. H. Lee, W. S. Jung, J. Vučković, M. L. Brongersma and K. C. Saraswat: Nano Lett. **13** (7) (2013) 3118.

67) M. J. Suess, R. Geiger, R. A. Minamisawa, G. Schiefler, D. C. J. Frigerio, G. Isella, R. Spolenak, J. Faist and H. Sigg: Nature Photonics **7** (2013) 466.

68) D. S. Sukhdeo, D. Nam, J. H. Kang, M. L. Brongersma and K. C. Saraswat: Photon. Res. **2** (3) (2014) A8.

69) Y. Suwa and S. Saito: *IEEE 8th Int. Conf. Group IV Photonics* 2011) p. 222.

70) K. Tani, S. Saito, Y. Lee, K. Oda, T. Mine, T. Sugawara and T. Ido: Jpn. J. Appl. Phys. **51** (2012) 04DG09.

71) K. Oda, K. Tani, S. Saito and T. Ido: ECS Transactions **50** (2012) 277.

72) K. Oda, T. Okumura, K. Tani, S. Saito and T. Ido: Thin Solid Films **557** (2014) 355.

73) K. Oda, K. Tani, S.-i. Saito and T. Ido: Thin Solid Films **550** (2014) 509.

74) L. T. Canham: Appl. Phys. Lett. **57** (1990) 1046.

75) N. Koshida and H. Koyama: Appl. Phys. Lett. **60** (1992) 347.

76) S. Fukatsu, N. Usami, T. Chinzei, Y. Shiraki, A. Nishida and K. Nakagawa: Jpn. J. Appl. Phys. **31** (1992) L1015.

77) B. Gelloz and N. Koshida: J. Appl. Phys. **88** (7) (2000) 4319.

78) A. Ghrib, M. E. Kurdi, M. de Kersauson, M. Prost, S. Sauvage, X. Checoury, G. Beaudoin, I. Sagnes and P. Boucaud: Appl. Phys. Lett. **102** (22) (2013) 221112.

79) A. Ghib, M. E. Kurdi, M. Prost, S. Sauvage, X. Checoury, G. Beaudoin, M. Chaigneau, R. Ossikovski, I. Sagnes and P. Boucaud: Adv. Optical Mater. **3** (2015) 353.

80) R. Geiger, T. Zabel and H. Sigg: Front. Mat. **2** (2015) 52.

81) S. Saito, K. Oda, T. Takahama, K. Tani and T. Mine: Appl. Phys. Lett. **99** (24) (2011) 241105.

82) S. Saito, F. Y. Gardes, A. Z. Al-Attili, K. Tani, K. Oda, Y. Suwa, T. Ido, Y. Ishikawa, S. Kako, S. Iwamoto and Y. Arakawa: Front. Mat.

83) S. Saito, A. Z. Al-Attili, K. Oda and Y. Ishikawa: Semicond. Sci. Technol. **31** (2016) 043002.

84) P. Boucaud, M. E. Kurdi, A. Ghrib, M. Prost, M. de Kersauson, S. Sauvage, F. Aniel, X. Checoury, G. Beaudoin, L. Largeau, I. Sagnes, G. Ndong, M. Chaigneau and R. Ossikovski: Photon. Res. **1** (3) (2013) 102.

85) L. Allen, M. W. Beijersbergen, R. J. C. Spreeuw and J. P. Woerdman: Phys. Rev. A **45** (1992) 8185.

86) L. Allen and M. J. Padgett: Opt. Comm. **184** (2000) 67.

87) M. J. Padgett and J. Courtial: Opt. Lett. **24** (1999) 430.

88) S. M. Barnett, L. Allen, R. P. Cameron, C. R. Gilson, M. J. Padgett, F. C. Speirits and A. M. Yao: J. Opt. **18** (2016) 064004.

89) S. M. Barnett, M. Babiker and M. J. Padgett: Phil. Trans. R. Soc. A **375** (2016) 20150444.

90) K. Y. Bliokh, F. J. Rodríguez-Fortuño, F. Nori and A. V. Zayats: Nat. Photon. **9** (2015) 796.

91) K. Y. Bliokh, A. Y. Bekshaev and F. Nori: Phys. Rev. Lett. **119** (2017) 073901.

92) K. Y. Bliokh, A. Y. Bekshaev and F. Nori: New J. Phys. **19** (2017) 123014.

93) Y. Kokubun: Jpn. J. Appl. Phys. **57** (2018) 08pA05.

94) D. A. B. Miller: Opt. Exp. **20** (2012) A293.

95) R. People: IEEE J. Selec. Top. Quant. Elec. **22** (1696-1710).

96) F. Y. Gardes, D. J. Thomson, N. G. Emerson and G. T. Reed: Opt. Exp. **19** (11804–11814).

97) D. J. Thomson, F. Y. Gardes, S. Liu, P. H, L. Zimmermaann, J. M. Fedeli, Y. Hu, M. Nedeljkovic, X. Yang, P. Petropoulos and G. Z. Mashanovich: J. Sel. Top. Quant. Electron. **19** (2013) 3400510.

98) X. Wu, B. Dama, P. Gothoskar, P. Metz, K. Shastri, S. Sunder, J. V. d. Spiegel, Y. Wang, M. Webster and W. Wilson: IEEE Int. Solid-State Circuits Conf. (ISSCC) (2013) 7.7.

99) S. Akiyama and T. Usuki: Front. Phys. **2** (2014) 65.

100) J. Fujikata, S. Takahashi, M. Takahashi and T. Horikawa: IEEE Group-IV Photonics (GFP) (2013) ThA4.

101) S. Ren, Y. Rong, T. I. Kamins, J. S. Harris and D. A. B. Miller: Appl. Phys. Lett. **98** (2011) 151108.

102) S. Ren, Y. Rong, A. C. adn R. K. Schaevitz, T. I. Kaminis, J. S. Harris and D. A. B. Miller: IEEE J. Photon. Technol. Lett. **24** (2011) 461.

103) D. Feng, S. Liao, H. Liang, J. Fong, B. Bijlani, R. Shafiiha, B. J. Luff, Y. Luo, J. Cunningham, A. V. Krishnamoorthy and M. Asghari: Opt. Exp. **20** (2012) 22224.

104) P. Chaisakul, D. Marris-Morini, M. S. Rouifed, G. Isella, D. Chrastina, J. Frigerio, X. L. Roux, S. Edmond, J. R. Coudevylle and L. Vivien: Opt. Exp. **20** (2012) 3219.

105) J. Liu, M. Beals, A. Pomerene, S. Bernardis, R. Sun, J. Cheng, L. C. Kimerling and J. Michel: Nat. Photon. **2** (2008) 433.

106) M. R. Watts, W. A. Zortman, D. C. Trotter, R. W. Young and A. L. Lentine: Opt. Exp. **19** (2011) 21989.

107) Q. Xu, S. Manipatruni, B. Schmidt, J. Shakya and M. Lipson: Opt. Exp. **15** (2007) 430.

108) G. T. Reed, G. Mashanovich, F. Y. Gardes and D. J. Thomson: Nat. Photon. **4** (2010) 518.

109) K. Iga: Jpn. J. Appl. Phys. **57** (2018) 08PA01.

110) T. Baehr-Jones, T. Pinguet, P. L. Guo-Qiang, S. Danziger, D. Prather and M. Hochberg: Nat. Photon. **6** (2012) 206.

111) D. Hisamoto, W. Lee, J. Kedzierski, H. Takeuchi, K. Asano, C. Kuo, E. Anderson, T. King, J. Bokor and C. Hu: IEEE Trans. Electron Devices **47** (12) (2000) 2320.

112) R. Palmber, L. Alloatti, D. Korn, P. C. Schindler, M. Baier, J. Bolten, T. Wahlbrink, M. Waldow, R. Dinu, W. Freude, C. Koos and J. Leuthold: IEEE Photon. Tech. Lett **25** (2013) 1226.

113) L. Alloatti, D. Korn, R. Palmer, D. Hillerkuss, J. Li, A. BBarklund, R. Dinu, J. Wieland, M. Fournier, J. Fedeli, H. Yu, W. Bogaerts, P. Dumon, R. Baets, C. Koos, W. Freude and J. Leuthold: Opt. Exp, **19** (2011) 11841.

114) Z. Ren, P. J. Heard, J. M. Marshall, P. A. Thomas and S. Yu: J. Appl. Phys. **103** (2008) 034109.

115) C. Wang, M. Zhang, X. Chen, M. Bertrand, A. Shams-Ansari, S. Chandrasekhar, P. Winzer and M. Loncar: Nature **562** (2018) 101.

116) Z. Zhou, R. Chen, X. Li and T. Li: Opt. Fiber Tech. **44** (2018) 13.

117) M. He, M. Xu, Y. Ren, J. Jian, Z. Ruan, Y. Xu, S. Gao, S. Sun, X. Wen, L. Zhou, L. Liu, C. Guo, H. Chen, S. Yu, L. Liu and X. Cai:

Nat. Photon. **13** (2019) 359.

118) R. Wu, M. Wang, J. Xu, J. Qi, W. Chu, Z. Fang, J. Zhang, J. Zhou, Q. L, Z. Chai, J. Lin and Y. Cheng: Nanomaterials **8** (2018) 910.

119) T. Usui, C. A. Donnelly, M. Logar, R. Sinclair, J. Schoonman and F. B. Prinz: Acta Mater. **61** (2013) 7660.

120) V. M. Mordvintsev, S. E. Kudryavtsev and V. L. Levin: Tech. Phys. **63** (2018) 1681.

121) A. Namba, M. Sugimoto, T. Ogura, Y. Tomita and K. Eda: Appl. Phys. Lett. **67** (1995) 3275.

122) P. O. Weigel, M. Savanier, C. T. DeRose, A. T. Pomerene, A. L. Starbuck, A. L. Lentine, V. Stenger and S. Mookherjea: Sci. Rep. **6** (2016) 22301.

123) O. Mitomi, K. Noguchi and H. Miyazawa: IEEE Proc. Optoelectron. **145** (1998) 360.

124) : *Lumerical Mode Solutions®: https://www.lumerical.com* .

125) G. D. Boyd, W. L. Bond and H. L. Carter: J. Appl. Phys. **38** (1967) 1941.

126) H. H. Li: J. Phys. Chem. Ref. Data **9** (1980) 561.

127) C. Z. Tan and J. Amdt: J. Phys. & Chem. Solid. **61** (2000) 1315.

128) : *COMSOL Multiphysics®: https://www.comsol.com* .

129) L. Alloatti, R. Palmer, S. Diebold, K. P. Pahl, B. Chen, R. Dinu, M. Fedeli, T. Zwick, W. Freude, C. Koos and J. Leuthold: Light: Science & Appl. **3** (2014) e173.

130) E. Ip, A. P. T. Lau, D. J. F. Barros and J. M. Kahn: Opt. Exp. **16** (2008) 753.

131) J. D. Jannopoulos and R. D. M. J. N. Winn: *Photonic Crystals* (Princeton University Press, Princeton, 1995).

132) T. F. Krauss, R. M. D. L. Rue and S. Brand: Nature **384** (1996) 699.

133) J. J. Sakurai and J. J. Napolitano: *Modern Quantum Mechanics* (Pearson, 2014).

134) J. J. Sakurai: *Advanced Quantum Mechanics* (Addison-Wesley Publishing Company, 1967).

135) J. Bardeen, L. N. Cooper and J. R. Schrieffer: Phys. Rev. **108** (1957) 1175.

136) J. R. Schrieffer: *Theory of Superconductivity* (Westview Press, 1971).

137) P. W. Anderson: Phys. Rev. **112** (1958) 1900.

138) Y. Nambu: Phys. Rev. **117** (648–663).

139) P. W. Higgs: Phys. Lett **12** (1962) 132.

140) J. Goldstone, A. Salam and S. Weinberg: Phy. Rev. **127** (1962) 965.

141) A. Einstein and J. Laub: Annalen der Physik **26** (1908) 532.

142) G. Baym: *Lectures on Quantum Mechanics* (Westview Press, 1969).

143) N. Nagaosa: *Quantum Field Theory in Condensed Matter Physics* (Springer, 1999).

144) X. G. Wen: *Quantum Field Theory of Many-Body Systems* (Oxford University Press, 2004).

145) J. H. Poincaré: *Théorie mathématique de la lumière* (G. Carré, 1892).

146) G. G. Stokes: Trans. Cambridge Phil. Soc. **9** (1851) 399.

147) R. C. Jones: J. Opt. Soc. Am. **31** (1941) 488.

148) J. D. Jackson: *Classical Electrodynamics* (John Wiley & Sons, 1999).

149) D. H. Goldstein: *Polarized Light* (CRC Press, 2011).

150) J. J. Gil and R. Ossikovski: *Polarized Light and the Mueller Matrix Approach* (CRC Press, 2016).

151) K. Kasamatsu, I. Ichinose and T. Matsui: Phys. Rev. Lett. **111** (2013) 115303.

152) M. Lehner: *The Cambridge Companion to Einstein (Cambridge Companions to Philosophy)* (Cambridge University Press, 2014).

153) S. J. v. Enk and G. Nienhuis: J. Mod. Opt. **41** (1994) 963.

154) X. S. Chen, X. F. Lu, W. M. Sun, F. Wang and T. Goldman: Phys. Rev. Lett. **100** (2008) 232002.

155) X. Ji: Phys. Rev. Lett. **104** (2010) 039101.

156) E. Leader and C. Lorcé: Phys. Rep. **541** (2014) 163.

157) : *The data from the paper can be obtained from the University of Southampton ePrint research repository: https://doi.org/10.5258/SOTON/D0950, 10.5258/SOTON/D0305, 10.5258/SOTON/D0760, and 10.5258/SOTON/D0671* .